

Spectroscopy of two-dimensional interacting lattice electrons using symmetry-aware neural backflow transformations

Imelda Romero, Jannes Nys, and Giuseppe Carleo

Institute of Physics, École Polytechnique Fédérale de Lausanne (EPFL), CH-1015 Lausanne, Switzerland and Center for Quantum Science and Engineering, École Polytechnique

Fédérale de Lausanne (EPFL), CH-1015 Lausanne, Switzerland

(Dated: June 14, 2024)

Neural networks have shown to be a powerful tool to represent ground state of quantum many-body systems, including for fermionic systems. In this work, we introduce a framework for embedding lattice symmetries in Neural Slater-Backflow-Jastrow wavefunction ansatzes, and demonstrate how our model allows us to target the ground state and low-lying excited states. To capture the Hamiltonian symmetries, we introduce group-equivariant backflow transformations. We study the low-energy excitation spectrum of the t - V model on a square lattice away from half-filling, and find that our symmetry-aware backflow significantly improves the ground-state energies, and yields accurate low-lying excited states for up to 10×10 lattices. We additionally compute the two-point density-correlation function and the structure factor to detect the phase transition and determine the critical point. Finally, we quantify the variational accuracy of our model using the V -score.

I. INTRODUCTION

Strong correlations lead to rich physical phenomena in quantum many-body systems, such as metal-insulator transitions, spin-charge separation, and the paradigmatic fractional quantum hall effect [1–4]. The strong interactions among particles in these systems make their description complex. Various numerical methods have been developed to tackle the strongly correlated regime, including variational approaches such as variational Monte Carlo (VMC) [5] and tensor network methods [6]. Machine learning has recently found its application in quantum many-body physics to introduce flexible and powerful parameterizations of quantum states. This is guided by the capacity of neural networks to act as universal and efficient high-dimensional function approximators [7]. They have shown great potential, often resulting in state-of-the-art ground state approximations, especially in 2D [8–13], and have also found their application in dynamics [7, 14–20].

Neural network quantum states (NQS) [7] have also been used to simulate fermionic systems in the first and second quantization formalisms [21–27]. In the latter, the fermionic anticommutation relations make variational approaches challenging. This is particularly clear when mapping fermionic operators onto spin operators, e.g. using Jordan-Wigner in >1 D, where these mappings introduce a highly non local spin Hamiltonian [28]. On the other hand, in the first quantization formalism one must exactly fulfill the particle-permutation antisymmetry of the wave function. A conventional variational wavefunction typically involves a (mean-field) Slater determinant to account for antisymmetry, combined with a two-body Jastrow factor [29] to capture particle correlations. One way to further improve this ansatz is by introducing correction terms known as backflow transformations (BF). This modification involves making the orbitals within the Slater determinant depend on the positions of all fermions. Feynman and Cohen originally

introduced the idea to analyze the excitation spectrum of liquid Helium-4 [30], and was successfully extended to electronic degrees of freedom [31–35]. Backflow transformations can alter the nodal surface, thereby reducing approximation errors [32, 36–38]. Recently, the backflow transformation has been introduced as a neural network in the context of NQS applied to discrete [39] and continuous [26, 27] fermionic systems.

For spin degrees of freedom, it has been demonstrated that embedding symmetries into NQS can greatly improve ground state accuracy [13, 21, 40–46]. Furthermore, restoring the symmetries of the system enables us to target low-lying excited states that can be classified by the different symmetry sectors [21, 40]. One general way to target the low-energy states of the symmetry sectors is by applying quantum-number projectors to the wave function [21].

In this work, we introduce a method for embedding lattice symmetries of 2D fermionic lattice Hamiltonians into neural backflow transformations and demonstrate its efficacy using Slater-Backflow-Jastrow wavefunction ansatzes. We benchmark our ansatz on the t - V model on a square lattice and find that it significantly increases the ground-state accuracy compared to other state-of-the-art approaches, and additionally allows us to accurately determine the low-lying excited states over a wide range of interaction strengths.

II. METHODS

A. Fermions on the lattice

Consider a system of fermions that reside on a lattice represented by an undirected graph $\mathcal{G} = (\mathcal{V}, \mathcal{E})$, with a set of vertices denoted \mathcal{V} and undirected edges as \mathcal{E} . Each lattice site is labeled $i \in \mathcal{V}$, and the total number of sites is $N_s = |\mathcal{V}|$. To each vertex i we associate a position vector \mathbf{r}_i . The total number of fermions is conserved and will

be fixed at $N_f \leq N_s$, and the particle density is defined as $\bar{n} = \frac{N_f}{N_s}$. We introduce the creation and annihilation operators of the fermionic mode (or lattice site) i as \hat{c}_i^\dagger and \hat{c}_i , respectively, and do not consider the spin of the fermions. These operators respect the usual fermionic anticommutation relations. In addition, we also introduce the corresponding number operator $\hat{n}_i = \hat{c}_i^\dagger \hat{c}_i$.

It will prove useful to connect the two main formalisms for describing fermionic systems: first quantization, which labels the fermions, and second quantization where we consider the occupation number basis or a given orbital set (here the lattice sites). To establish the correspondence, we consider a canonical ordering of the lattice sites through their label assignment $i = \{1, \dots, N_s\}$. The latter can be chosen arbitrarily, and in practice we choose a snake-like ordering in the case of the 2D lattice. This enables us to recover the particle positions in the first quantization framework from a given occupation number configuration in second quantization (see Ref. [22]). We introduce $x = (\mathbf{r}_{i_1}, \mathbf{r}_{i_2}, \dots, \mathbf{r}_{i_{N_f}})$, where i_p is the site index occupied by the p^{th} electron, where the fermion number index is determined by the chosen canonical ordering. In other words, we have an ordered set of indices $i_1 < i_2 < \dots < i_{N_f}$. Furthermore, we introduce the occupation number configuration $n = (n_1, \dots, n_{N_s}) \in \{0, 1\}^{N_s}$. Hence, in this notation, the canonical ordering allows us to extract active or occupied lattice indices $\{i_p\}_{p=1, \dots, N_f}$, given the occupation numbers n . This establishes implicit mappings $x = x(n)$ and $n = n(x)$ (see Fig. 1).

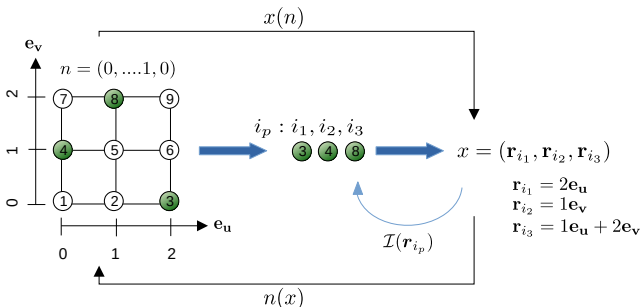


FIG. 1. Implicit mappings of $x(n)$ and $n(x)$. This figure shows how the occupation configuration $n = (n_1, \dots, n_{N_s}) = (0, 0, 1, 1, 0, 0, 0, 1, 0)$ maps to the position vectors $x = (\mathbf{r}_{i_1}, \mathbf{r}_{i_2}, \dots, \mathbf{r}_{i_{N_f}})$, and vice versa, illustrating the relationship between occupied lattice sites and their indices respecting a canonical ordering.

B. Wavefunction ansatz

1. Slater-Jastrow

Consider a set of N_f single-particle mean-field (MF) orbitals $\{\phi_\mu(\mathbf{r})\}_{\mu=1, \dots, N_f}$ evaluated at position \mathbf{r} . For

convenience, we introduce the matrix $M \in \mathbb{C}^{N_f \times N_s}$, with elements defined as

$$M_{\mu,i} = \phi_\mu(\mathbf{r}_i), \quad (1)$$

for all N_s sites i . For a given set of particle positions x , we define the reduced matrix $\bar{M} \in \mathbb{C}^{N_f \times N_f}$ by selecting the columns of M corresponding to the occupied sites: $\bar{M} = M_{\mu,i_p}$, where i_p are the lattice sites that are occupied by particle $p \in \{1, \dots, N_f\}$.

The mean-field Slater determinant can be dressed with a Jastrow factor that introduces two-body correlations, and we obtain:

$$\psi(n) = \det \bar{M} \cdot e^{J(n)}. \quad (2)$$

The two-body Jastrow factor is defined as [29, 47]

$$J(n) = \frac{1}{2} \sum_{ij} n_i W_{d(ij)} n_j, \quad (3)$$

where the subscript $d(ij)$ of the complex variational parameters W denotes the distance between site i and j .

2. Neural Backflow Transformation

The Slater-Jastrow wavefunction ansatz can be further improved by including backflow transformations, thereby significantly increasing the expressiveness of the model. We use the neural backflow transformation that effectively promotes the single-particle orbitals to many-body orbitals [26, 27, 39]. Therefore, we introduce the backflow function F that produces a configuration-dependent orbital matrix $F \in \mathbb{C}^{N_f \times N_s}$. We then adapt the orbital matrix as

$$M_{\mu,i} \rightarrow B_{\mu,i}(n) = M_{\mu i} \circ F_{\mu i}(n), \quad (4)$$

where \circ corresponds to an element-wise product between the matrices \bar{M} and F . The corresponding reduced matrix of B is \bar{B} , and is obtained similarly as for \bar{M} . The Neural Slater-Backflow-Jastrow ansatz is then defined as

$$\psi_{BF}(n) = \det \bar{B}(n) \cdot e^{J(n)}. \quad (5)$$

Below, we will describe the properties of the backflow function F and introduce a neural parametrization thereof.

C. Symmetries and Excitations

We consider an electronic Hamiltonian on a lattice that commutes with the elements of a symmetry group G , such as total spin, the total momentum, and geometrical symmetries such as rotation. The eigenstates of these the many-body Hamiltonian can be classified with the symmetry sectors of G . We restrict the NQS ansatz to a

given symmetry sector labeled by I through a quantum-number projection

$$\psi^I(n) = \sum_{g \in G} \chi_g^{I*} \psi(\hat{g}^{-1}n), \quad (6)$$

and χ_g^I is the character corresponding to the irreducible representation (irrep) I and group element g . To make the notation more explicit, consider a translation operator denoted by $\hat{g} = \hat{T}_\tau$, where τ is the corresponding translation vector. The effect of the operator on a configuration n is to permute the site indices $(1, \dots, N_s) \rightarrow (\tau_1, \dots, \tau_{N_s})$, i.e. $\hat{T}_\tau |n\rangle = |n_{\tau_1}, \dots, n_{\tau_{N_s}}\rangle$ where in terms of the position map $n_{\tau_i} = n(\mathbf{r}_i - \tau)$. In this work we focus on the projected form

$$\psi^K(n) = \sum_{\tau} e^{-i\tau \cdot \mathbf{K}} \psi(\hat{T}_\tau^{-1}n), \quad (7)$$

where \mathbf{K} is the total momentum and the sum runs over all possible translation vectors. We use the above-mentioned quantum number projection to compute both the ground state and the low-lying excited states. The low-lying excitations are characterized by different momentum sectors, and their computation involves optimizing the wavefunction within the quantum number sectors distinct from the ground state [43, 45]. Instead of focusing on a single excited state individually, an alternative strategy involves adopting a multi-target approach, which has recently been introduced for continuous systems [48]. However, for cost-effectiveness and interpretation in terms of translation quantum numbers, we focus on the symmetry-projection method outlined above.

In a brute-force approach, the evaluation of the symmetrized wave function $\psi^I(n)$ for a configuration n would require $|G|$ evaluations of the parametrized non-symmetric wave function ψ in Eq. (6). In particular, for translation symmetry in Eq. (7) of a square lattice of size $L \times L$, this would require $|G| = L^2$ evaluations. The computational burden induced by the symmetrization procedure can therefore become significant for increasing system sizes. For this purpose, we introduce a novel set of *symmetry-aware neural backflow transformations* that require only a single evaluation of a neural network to produce *all* $\psi(\hat{g}^{-1}n)$ (i.e. $\forall g \in G$) required to evaluate the projection in Eq. (6). This will allow us to reach larger system sizes, even when considering deep neural networks to represent the backflow transformation. In the next section, we discuss the requirements of this symmetry-aware backflow transformation and introduce a specific neural parametrization to fulfill the constraints.

1. Equivariance Condition

We will introduce backflow transformations that keep both the particle-permutation and lattice symmetries

manifest, by introducing transformations that are equivariant under the respective groups. More concretely, when two fermions p and q are exchanged by the permutation operator \hat{P}_{pq} or when a lattice-symmetry transformation \hat{g} is applied to the lattice, the respective outputs of the neural backflow change accordingly:

$$F_{\mu, i_p}(\hat{P}_{pq}^{-1}n) \stackrel{!}{=} F_{\mu, \hat{P}_{pq}i_p}(n) = F_{\mu, i_q}(n), \quad (8)$$

$$F_{\mu, i_p}(\hat{g}^{-1}n) \stackrel{!}{=} F_{\mu, \hat{g}i_p}(n). \quad (9)$$

In the case of translations we enforce $F_{\mu, i_p}(\hat{T}_\tau^{-1}n) = F_{\mu, \hat{T}_\tau i_p}(n) = F_{\mu, \mathcal{I}(\mathbf{r}_{i_p} + \tau)}$, where $\mathcal{I}(\mathbf{r}_{i_p} + \tau)$ (defined in Fig. 1) denotes the index of the lattice site obtained by shifting \mathbf{r}_{i_p} by the translation vector τ . In other words, lattice symmetries can be defined by their permutation of the lattice sites.

Our key objective is to preserve translation equivariance in the backflow transformation. Using this, we can construct a symmetrized Neural Slater-Backflow-Jastrow ansatz, given that the Jastrow correlation function is translation-invariant and the backflow is constructed as a neural network respecting the equivariance conditions in Eqs. (8) and (9). A natural candidate for a symmetry-equivariant neural network is a convolutional neural network (CNN) operating on occupation configurations [49–51], which naturally exhibits these properties. In a CNN, spatial translations in the input lead to corresponding shifts in the output feature maps. The occupation configurations undergo multiple CNN-transformation layers, resulting in an output of the same size L^2 as the input configuration. We employ N_f independent backflow transformations corresponding to the different orbitals μ . From the outputs, we obtain the reduced matrix \bar{B} in Eq. (5), by selecting the columns corresponding to the occupied sites from the resulting backflow matrix $F_{\mu, i}(n)$. We depict this procedure in Fig. 2 where we provide a visual representation of a CNN backflow satisfying the equivariance conditions. In summary, given our CNN backflow is equivariant: instead of evaluating the CNN for all elements of the translation symmetry group, we can extract all the required $\psi(\hat{g}^{-1}n)$ in Eq. (6) from the output of a single evaluation of the backflow CNN. This approach improves efficiency and reduces computational redundancy in handling symmetrical transformations. In Fig. 2 we explicitly show this symmetry-averaging process under equivariance conditions. For additional information on the architecture and its adaptation to different system sizes, we refer to Appendix A.

III. RESULTS

A. Hamiltonian and Observables

The Hamiltonian of the t - V model reads

$$\hat{H} = -t \sum_{(i,j) \in \mathcal{E}} \hat{c}_i^\dagger \hat{c}_j + \hat{c}_j^\dagger \hat{c}_i + V \sum_{(i,j) \in \mathcal{E}} \hat{n}_i \hat{n}_j. \quad (10)$$

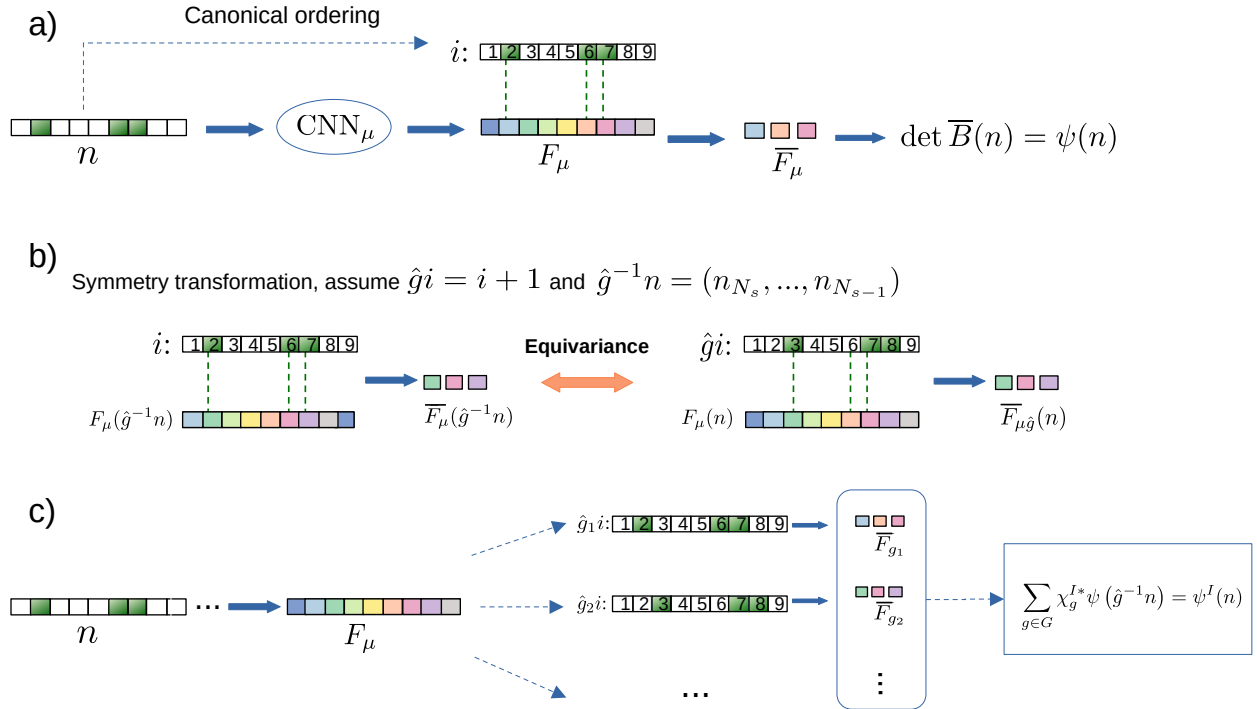


FIG. 2. Visual representations of the symmetry-aware backflow, the translational equivariance condition, and the quantum number projection. Panel **a)** showcases how the backflow determinants are constructed. The neural network CNN_μ for a given orbital μ takes as input the configuration n , and produces a backflow vector output $F_\mu(n)$. The reduced matrix \bar{F}_μ is obtained by selecting the active indices i from F_μ . These active indices are linked to the occupied sites, represented by the dark green blocks in the input n , using the canonical ordering. Panel **b)** demonstrates the equivariance property of the backflow function. Applying a symmetry transformation to the input as $\hat{g}^{-1}n$ and then extracting the active indices, we get $\bar{F}_\mu(\hat{g}^{-1}n)$. This is equivalent to applying the symmetry transformation directly to the active indices represented by $\hat{g}i$. This results equivalently in the reduced matrix $\bar{F}_{\mu\hat{g}}(n)$. Panel **c)** represents the quantum number projection. Following a single CNN evaluation, we obtain the reduced matrices $\bar{F}_{\mu g}, \forall \hat{g} \in G$ by properly constructing the reduced matrix, without reevaluating the backflow CNN. Subsequently, we compute the symmetry-averaged wavefunction $\psi(\hat{g}^{-1}n)$.

The first term describes electron hopping between neighboring sites with hopping parameter t . The second term corresponds to the nearest neighbor Coulomb repulsion with interaction strength $V \geq 0$. We will set $t = 1$ from hereon. We further decompose the Hilbert space \mathcal{H} into fixed particle-number subspaces \mathcal{H}_{N_f} [52]. The t - V model was originally introduced to study the thermodynamic and transport properties of superconductors [53, 54]. Additionally, it provides a conceptual framework for explaining phenomena such as phase separation or stripe order in cuprates and organic conductors [55–60]. In practice, the t - V model can be realized, for example, in experiments with strongly polarized ^3He atoms [61, 62]. Despite its apparent simplicity, the t - V model cannot be solved analytically in two or higher dimensions. It also reveals highly nontrivial phase transitions that have been studied in previous works with various computational techniques, including variational Monte Carlo [22, 55, 63–70].

In the strong-coupling limit where $V/t \rightarrow \infty$ we encounter a charge-ordering (CO) phase where the system

behaves classical. At large V/t , it is energetically unfavorable for two fermions to occupy neighboring lattice sites. The correlations become short-ranged, suggesting localization and insulating behavior, giving rise to a charge-ordered insulating phase. At half-filling ($\bar{n} = 0.5$) the charge order corresponds to a checkerboard pattern. Conversely, at weak interaction strengths V/t , the fermions can easily hop between neighboring lattice sites, and the system behaves like a non-interacting free Fermi gas. In this weak coupling limit the system enters the metallic phase and becomes exactly solvable at $V/t \rightarrow 0$ [22, 63, 64, 71–76].

We introduce the normalized density-density correlation function as [22]

$$C(R) = \frac{1}{|\mathcal{V}||S_R|} \sum_{i \in \mathcal{V}} \sum_{j \in S_R(i)} \langle (\hat{n}_i - \bar{n})(\hat{n}_j - \bar{n}) \rangle \quad (11)$$

where $S_R(i) = \{j \in \mathcal{V} : d(i, j) = R\}$ is the set of vertices with a fixed distance R from the vertex i . Another important observable to detect the CO phase is the structure

factor [63, 64, 66, 67, 77]:

$$S(\mathbf{K}) = \frac{1}{N} \sum_{j,k \in \mathcal{V}} e^{i\mathbf{K} \cdot (\mathbf{r}_j - \mathbf{r}_k)} \langle (\hat{n}_j - \bar{n}) (\hat{n}_k - \bar{n}) \rangle. \quad (12)$$

In the CO phase, well-defined peaks at $\mathbf{K} = (\pi, \pi)$ indicate a checkerboard charge pattern, and in the thermodynamic limit $S((\pi, \pi))/N_s$ converges to a finite value, reflecting long-range order. We will study the t - V model on a two-dimensional square lattice of side L and with periodic boundary conditions, for various system sizes $|\mathcal{V}| = L^2$ and different interaction strengths V/t , with densities close to half-filling and at closed momentum shells.

B. Ground States

We benchmark our symmetrized Neural Slater-Backflow-Jastrow (ψ_{BF}^K) ansatz with respect to a mean-field Slater determinant (which is equivalent to Hartree-Fock (HF)), a symmetrized Slater-Jastrow (ψ^K) without backflow, and a non-symmetrized Slater-Jastrow. Furthermore, we compare with ground state energies obtained with another state-of-the-art neural quantum state method (“Slater-Jastrow with an additional sign correction neural network”) from Ref. [22]. In Fig. 3 (a), we show results for a small system size ($L = 4$), allowing comparison to results obtained by exact diagonalization (ED). Mean-field Slater relative errors range from 10^{-3} to 10^{-1} , with accuracies decreasing at large interaction strengths V/t . Our symmetrized backflow ansatz consistently yields ground-state errors below 10^{-4} , also at higher values of V/t . We also observe that the symmetry-aware backflow transformation yields the most accurate ground-state energies over the whole interaction regime. For a larger system size ($L = 10$), shown in Fig. 3 (b), this trend is confirmed. The backflow corrections significantly lower the estimated ground-state energy across all coupling strengths. We compare the converged VMC energies with HF energies by computing the difference $E - E_{HF}$. Our results show that the backflow ansatz consistently provides lower energies across the full range of interaction strengths.

In Fig. 4 (a), we show the density-density correlation function as defined in Eq. 11 for $L = 10$ close to half-filling $\bar{n} = 0.44$ (see Appendix B for results on the 8×8 system). When the interaction strength increases, the correlations start to oscillate more pronouncedly as a result of the increasingly ordered charge distribution. In the CO phase, the amplitudes of the oscillations decrease more gradually with distance compared to that of the metallic phase. For weak couplings, the correlations barely oscillate and fade as the graph distance R increases.

To pinpoint the transition point in the thermodynamic limit, we use finite-size scaling. We study the structure factor $S(\pi, \pi)/N_s$ for various V/t . The critical transition

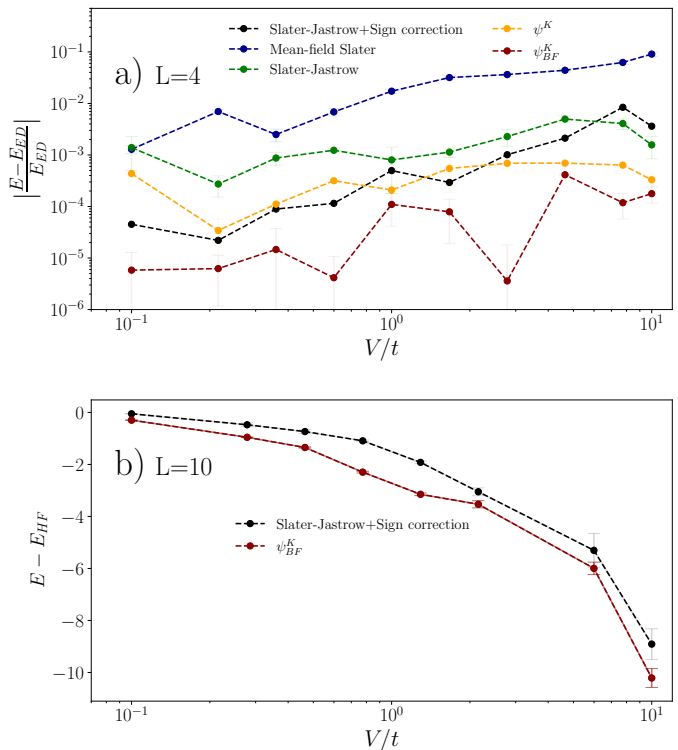


FIG. 3. Comparison of ground-state energies of the t - V model obtained with various wavefunction models. We evaluate the performance of our symmetrized Neural Slater-Backflow-Jastrow (ψ_{BF}^K) in comparison to a symmetrized Slater-Jastrow (ψ^K) without backflow, a non-symmetrized Slater-Jastrow, and the neural quantum state “Slater-Jastrow with an additional sign correction neural network” described in Ref. [22]. In panel a), we present results for $L = 4$ with $\bar{n} = 0.44$ and show relative errors compared to exact diagonalization (ED) as a function of the interaction strengths V/t . In panel b), we show the deviation from Hartree-Fock (HF) energies for a $L = 10$ system with filling fraction $\bar{n} = 0.44$ defined as $E - E_{HF}$.

V/t	S_∞
0.1	-0.026 ± 0.001
0.6	-0.021 ± 0.002
1.0	-0.003 ± 0.001
1.3	0.003 ± 0.001
1.6	0.042 ± 0.002
2.7	0.085 ± 0.002

TABLE I. Structure factor extrapolations to the thermodynamic limit (taken from Figure 4 (b)) as a function of V/t .

point is found where the structure factor attains a finite value in the thermodynamic limit. In Fig. 4 (b) we plot the structure factor $S(\pi, \pi)/N_s$ as a function of the size of the system $1/L$ (for $L = 4, 6, 8, 10$) and in Table I we report the extrapolated results in the thermodynamic limit. Near half-filling, specifically for $\bar{n} = 0.44$, we estimate that the transition occurs at $V_c/t \simeq 1.14 \pm 0.04$, which is consistent with the value reported in Ref. [22].

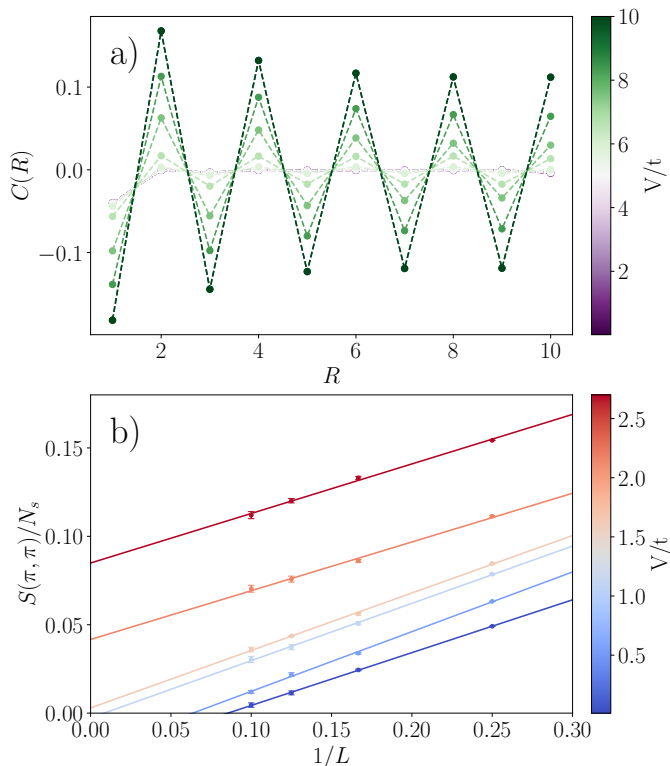


FIG. 4. **a)** The two-point density-density correlation functions as a function of graph distance R for different V/t for a system size of $L = 10$ and $\bar{n} = 0.44$. **b)** Finite-size scaling of the structure factor $S(\pi, \pi)/N_s$ versus different system sizes $1/L$ (where $L = 4, 6, 8, 10$) with $\bar{n} = 0.44$ for different values of V/t close to the estimated critical point $V_c/t \simeq 1.14 \pm 0.04$.

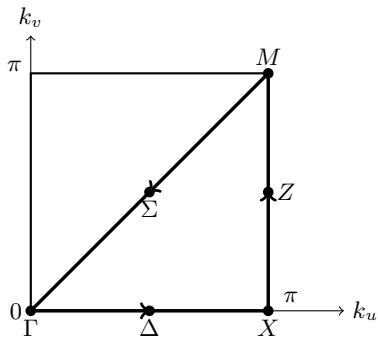


FIG. 5. Single quadrant of the first Brillouin zone of the two-dimensional square lattice with high-symmetry points (k_u, k_v) .

C. Excitations

To capture low-lying excitations, we carry out VMC optimizations across various momentum sectors $\mathbf{K} = (k_u, k_v)$, where $k_{u,v} = \{0, \pm \frac{2\pi m}{L_{u,v}}\}$, and $m = 1, \dots, \frac{L_{u,v}}{2}$. Here L_u and L_v are the side lengths of the two-dimensional lattice in the \mathbf{e}_u and \mathbf{e}_v directions. In Fig. 5,

we represent a single quadrant within the corresponding first Brillouin zone with conventional symbols to represent high-symmetry points [78].

We first benchmark the performance of our symmetrized Neural Slater-Backflow-Jastrow variational ansatz (ψ_{BF}^K) and a symmetrized Slater-Jastrow (ψ^K) (top) model for a system size of $L = 4$ and $\bar{n} = 0.31$ in Fig. 6. We observe that also in symmetry sectors different from the ground state, the symmetric backflow transformation reduces the relative energy error. We show the lowest energy state in each sector and compare it with results obtained from ED. In the lower panel of Fig. 6, we calculate the corresponding relative errors with respect to the ED energies. For our backflowed ansatz (ψ_{BF}^K) these lie between $10^{-6} - 10^{-3}$ for all sectors. In Appendix D, we also include additional simulation data of the open shell $L = 4$ system (see Fig. 13).

Prior studies have documented a range of coexistence phenomena for large and finite V/t away from half-filling, transitioning from phase separation to potential stripe and checkerboard coexistence. In Ref. [79], the t - V model on a square lattice with nearest-neighbor repulsive interactions was studied using mean-field theory for small system sizes. The authors observed a second-order phase transition from the Fermi liquid to the (π, π) charge density wave state. At stronger repulsion, charge density waves coexisted at different momentum sectors when doped away from half-filling. In Ref. [58] and the subsequent study in Ref. [59], exact diagonalization was used to study small 2D systems. They found that at high repulsion and around quarter-filling densities, doped holes formed stable charged stripes acting as anti-phase walls [80], which are stable against phase separation in fermionic systems.

We extend our analysis to larger system sizes $L = 8$ with $\bar{n} = 0.39$ and $L = 10$ with $\bar{n} = 0.41$ to reduce finite-size effects. We simulate each system size with distinct particle density to ensure the absence of ground-state degeneracies in the non-interacting limit. We confirm the persistent non-degenerate ground state at the $(0, 0)$ point (see Fig. 7 for $L = 8$ and Fig. 12 in Appendix C for $L = 10$). By comparing our symmetrized Neural Slater-Backflow-Jastrow (ψ_{BF}^K) ansatz with a symmetrized Slater-Jastrow (ψ^K) without backflow, we observe improved energy levels, even for low-lying excited states, with the inclusion of the backflow correction term.

In Fig. 8 we depict the gap between the ground state and the excited energy levels in different sectors for different V/t for both system sizes. We define the gap as the difference between the lowest energies in each sector relative to the lowest energy in the Γ sector:

$K = |E_0[\Gamma] - E_0[K]|$, where K corresponds to the symbols of different sectors (here $K = M, X$) and $E_0[K]$ is the lowest energy in given sector. Notably, for strong interactions, we consistently observe a smaller gap for M than for X . We include the gap K_∞ for the $V/t = \infty$ value in the plot for both system sizes. This demon-

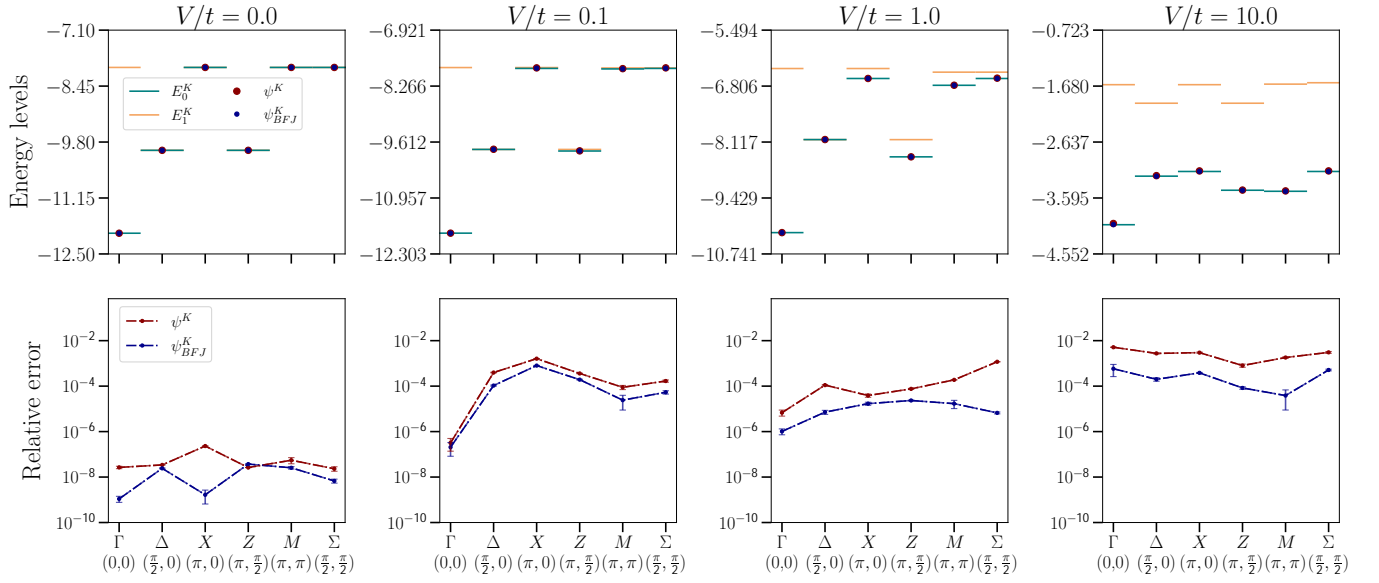


FIG. 6. (top panel) The lowest and second-lowest energies for the designated \mathbf{K} sector using ED, compared to the lowest energies in each sector, obtained with our variational ansatzes. (bottom panel) The relative energy errors associated with the ansatzes. These results are for a closed-shell system with $L = 4$ and a density of $\bar{n} = 0.31$.

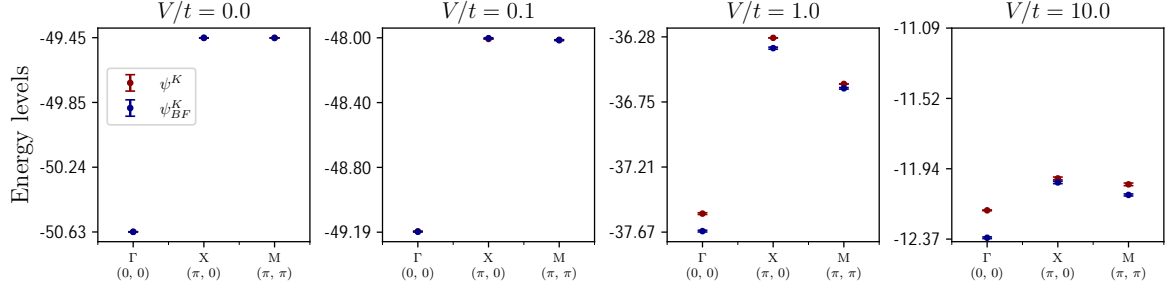


FIG. 7. Lowest excitation energies in different \mathbf{K} sectors for an $L = 8$ closed-shell system with $\bar{n} = 0.39$ across a range of V/t values.

strates a collapse in the interactions at infinite strength, indicating a charge-ordered phase where the electrons are fully localized. Furthermore, the gap between the lowest energy states in the M and X sectors appears largest in the intermediate coupling regime.

D. V-score

We now aim to generalize the assessment of the performance of our model. Since ED becomes intractable for larger system sizes, we rely on the recently introduced V-score as a guiding metric [81], which can be computed using the variational energy and its variance. The V-score is dimensionless and invariant under energy shifts by construction. It is defined as [81]:

$$\text{V-score} = \frac{N \text{Var } E}{(E - E_\infty)^2}, \quad (13)$$

where $N = N_f$ the number of degrees of freedom, $\text{Var } E$ is the variance, E is the variational energy and for the t - V model

$$E_\infty = \frac{V|\mathcal{E}|N_f(N_f - 1)}{N_s(N_s - 1)}, \quad (14)$$

where V is the interaction strength and $|\mathcal{E}|$ is the number of nearest neighbor bonds. The constant E_∞ is used to compensate for global shifts in the energy, depending on the definition of the Hamiltonian.

The V-score serves as a valuable tool for discerning which Hamiltonians and regimes pose challenges for arbitrary classical variational techniques, even when we lack prior knowledge about the precise exact solution. Its practicality lies in its ability to quantify the accuracy of a particular method independently, without the need for direct comparisons with other methods. In particular, this metric enables us to draw comparisons between the accuracy obtained with our method on the given Hamil-

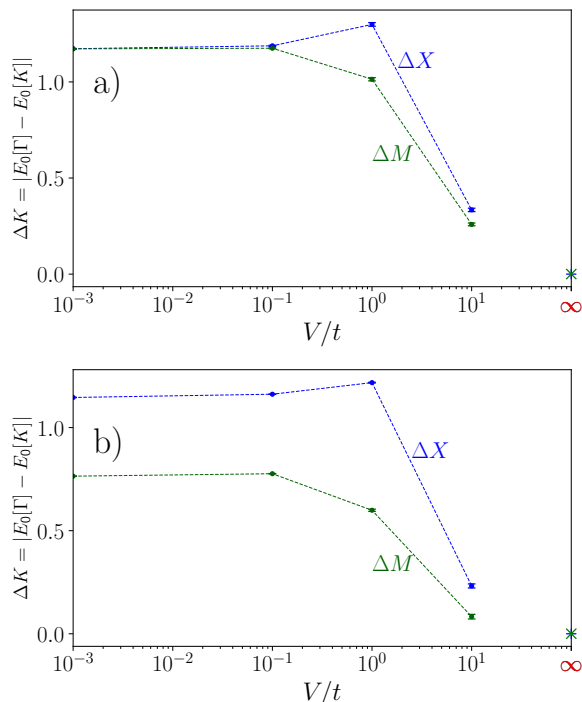


FIG. 8. Energy gaps ΔK between the ground state (located at the Γ point) and excitation energies ($K = M, X$) for **a)** $L = 8$ lattice with filling factor $\bar{n} = 0.39$ and **b)** $L = 10$ lattice with filling factor $\bar{n} = 0.41$, both being closed-shell systems with no ground state degeneracy. We include ΔK_∞ for $V/t = \infty$ in both figures, showing a collapse to a fully localized, charge-ordered phase at infinite repulsion.

tonian, compared to other commonly studied condensed matter Hamiltonians (including spin Hamiltonians).

In Fig. 9, we present the ground state V-scores for different ansatzes, including the symmetrized Neural Slater-Backflow-Jastrow (ψ_{BF}^K), symmetrized Slater-Jastrow (ψ^K) and Hartree-Fock (HF) ansatz, for system sizes $L = 4$ with $\bar{n} = 0.31$, and $L = 10$ with $\bar{n} = 0.41$. The data clearly illustrate a strong dependence of V-scores on the specific interaction regime under investigation. In particular, as the V score values increase, it becomes increasingly challenging to achieve accurate solutions using demanding variational algorithms, implying a greater level of difficulty in solving these systems accurately. Despite these challenges, we observe that the backflow ansatz consistently exhibits lower V-scores compared to other methods, indicating its more accurate performance.

Next, we analyze the V-scores of our backflow ansatz for ground states and excitations, as depicted in Fig. 10, across various scenarios and closed-shell system sizes ($L = 4$ with $\bar{n} = 0.31$, $L = 8$ with $\bar{n} = 0.39$, and $L = 10$ with $\bar{n} = 0.41$). We compute the scores across a range of interactions V/t . We observe that we obtain similar V-scores for excited states as for ground states at all system sizes and interaction strengths. This indicates that

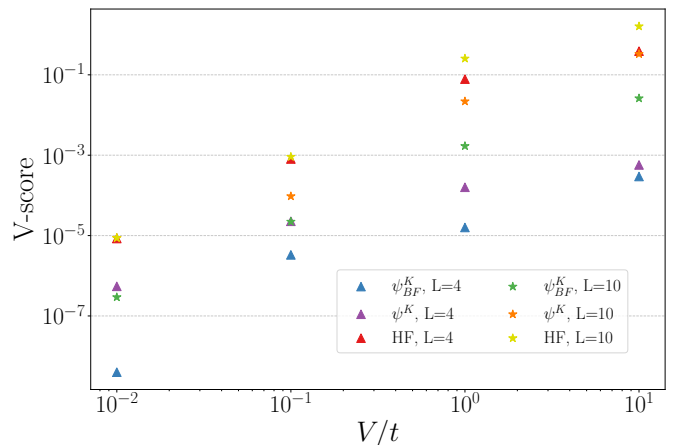


FIG. 9. Ground state V-scores comparison for different ansatz: ψ_{BF}^K (backflow), ψ^K (Slater-Jastrow), and HF (Hartree-Fock), across system sizes $L = 4$ with $\bar{n} = 0.31$, and $L = 10$ with $\bar{n} = 0.41$.

our results for excited states are highly accurate, even in the large V/t regime.

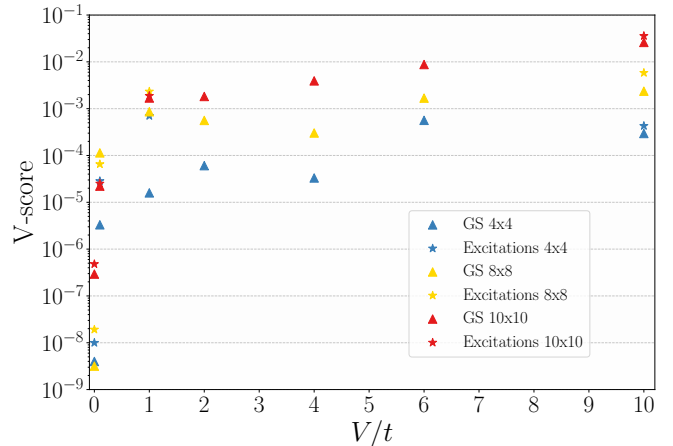


FIG. 10. V-score for a symmetrized Neural Slater-Backflow-Jastrow as a function of V/t for different ground (GS) and excited states for system sizes $L = 4$ with $\bar{n} = 0.31$, $L = 8$ with $\bar{n} = 0.39$, and $L = 10$ with $\bar{n} = 0.41$.

IV. CONCLUSION AND OUTLOOK

In this work, we introduced a novel approach to studying the low-energy excitation spectrum of fermionic Hamiltonians. By introducing symmetry-aware neural backflow transformations, we show that we can target the eigenstates of fermionic Hamiltonians with high accuracy. As a benchmark comparison, we show that this approach also yields significantly more accurate ground-state energies than other state-of-the-art variational Monte Carlo approaches.

In particular, we introduce equivariance conditions for the backflow transformations that lead to an efficient symmetry projection. We show that convolutional neural networks yield a powerful parametrization for our symmetry-aware backflow transformations that fulfill the equivariance conditions for both translation and particle-permutation symmetry. This key contribution enables us to efficiently access excited states by varying the total momentum \mathbf{K} in the quantum number projection. Furthermore, we have showcased the utility of our approach in identifying phase-transitions on the t - V model at system sizes far beyond what is reachable with exact diagonalization. To this end, we computed correlation functions and structure factors, resulting in the pinpointing of the critical point at $V_c/t = 1.14$. We also computed the V-score to quantify the variational accuracy of our proposed ansatz for different interaction regimes, system sizes and excitations. Previous analysis based on the V-score has highlighted the challenging nature of targeting fermionic eigenstates. Our observations indicate that the symmetry-aware backflow ansatz yields accurate ground states and performs favorably compared to other state-of-the-art methods over the full interaction regime, including when strong correlations occur. Additionally, we find that our method yields accurate approximations to the low-energy eigenstates with a given K

momentum.

Future extensions of our approach include generalizing it by including additional symmetries, such as rotational and reflection symmetries. This will involve using more general group-convolutional kernels, as in group-convolutional neural networks (GCNN) [49–51]. We focused on the nearest neighbor t - V model, but an extension is to consider Hamiltonians where spin-degrees of freedom become relevant as well (such as the Fermi-Hubbard model), or where interactions beyond nearest neighbor terms become relevant.

ACKNOWLEDGMENTS

We thank Dian Wu and Javier Robledo Moreno for engaging discussions. We especially thank Javier Robledo Moreno for sharing the data of Ref. [22]. We express our gratitude to Yusuke Nomura for providing valuable insights regarding quantum phase transitions and their connection to the structure of excitations. The open-source software NetKet version 3.9 was used to carry out the simulations [82, 83]. This work was supported by the Swiss National Science Foundation under Grant No. 200021_200336, and Microsoft Research.

-
- [1] J. Hubbard, Electron correlations in narrow energy bands iii. an improved solution, Proceedings of the Royal Society of London. Series A. Mathematical and Physical Sciences **281**, 401–419 (1964).
- [2] J. Vijayan, P. Sompet, G. Salomon, J. Koepsell, S. Hirtel, A. Bohrdt, F. Grusdt, I. Bloch, and C. Gross, Time-resolved observation of spin-charge deconfinement in fermionic hubbard chains, Science **367**, 186 (2020).
- [3] G. Li, W. Hanke, E. M. Hankiewicz, F. Reis, J. Schäfer, R. Claessen, C. Wu, and R. Thomale, Theoretical paradigm for the quantum spin hall effect at high temperatures, Physical Review B **98**, 10.1103/physrevb.98.165146 (2018).
- [4] A. Avella, Strongly correlated systems, Vol. 176 (Springer, 2013).
- [5] W. L. McMillan, Ground state of liquid he^4 , Phys. Rev. **138**, A442 (1965).
- [6] S. R. White, Density matrix formulation for quantum renormalization groups, Phys. Rev. Lett. **69**, 2863 (1992).
- [7] G. Carleo and M. Troyer, Solving the quantum many-body problem with artificial neural networks, Science **355**, 602 (2017).
- [8] G. Carleo, I. Cirac, K. Cranmer, L. Daudet, M. Schuld, N. Tishby, L. Vogt-Maranto, and L. Zdeborová, Machine learning and the physical sciences, Reviews of Modern Physics **91**, 10.1103/revmodphys.91.045002 (2019).
- [9] D.-L. Deng, X. Li, and S. D. Sarma, Quantum entanglement in neural network states, Physical Review X **7**, 10.1103/physrevx.7.021021 (2017).
- [10] J. Chen, S. Cheng, H. Xie, L. Wang, and T. Xiang, Equivalence of restricted boltzmann machines and tensor network states, Physical Review B **97**, 10.1103/physrevb.97.085104 (2018).
- [11] F. Ferrari, F. Becca, and J. Carrasquilla, Neural gutzwiller-projected variational wave functions, Physical Review B **100**, 10.1103/physrevb.100.125131 (2019).
- [12] M. Hibat-Allah, M. Ganahl, L. E. Hayward, R. G. Melko, and J. Carrasquilla, Recurrent neural network wave functions, Physical Review Research **2**, 10.1103/physrevresearch.2.023358 (2020).
- [13] Y. Nomura and M. Imada, Dirac-type nodal spin liquid revealed by refined quantum many-body solver using neural-network wave function, correlation ratio, and level spectroscopy, Phys. Rev. X **11**, 031034 (2021).
- [14] S. Czischek, M. Gärttner, and T. Gasenzer, Quenches near ising quantum criticality as a challenge for artificial neural networks, Phys. Rev. B **98**, 024311 (2018).
- [15] G. Fabiani and J. H. Mentink, Investigating ultrafast quantum magnetism with machine learning, SciPost Phys. **7**, 004 (2019).
- [16] M. Schmitt and M. Heyl, Quantum many-body dynamics in two dimensions with artificial neural networks, Phys. Rev. Lett. **125**, 100503 (2020).
- [17] G. Fabiani, M. D. Bouman, and J. H. Mentink, Supermagnonic propagation in two-dimensional antiferromagnets, Phys. Rev. Lett. **127**, 097202 (2021).
- [18] D. Hofmann, G. Fabiani, J. H. Mentink, G. Carleo, and M. A. Sentef, Role of stochastic noise and generalization error in the time propagation of neural-network quantum states, SciPost Phys. **12**, 165 (2022).
- [19] J. Nys, G. Pescia, and G. Carleo, Ab-initio variational wave functions for the time-dependent many-electron

- schrödinger equation (2024), arXiv:2403.07447 [cond-mat.str-el].
- [20] S.-H. Lin and F. Pollmann, Scaling of neural-network quantum states for time evolution, *physica status solidi (b)* **259**, 2100172 (2022).
- [21] K. Choo, A. Mezzacapo, and G. Carleo, Fermionic neural-network states for ab-initio electronic structure, *Nature Communications* **11**, 10.1038/s41467-020-15724-9 (2020).
- [22] J. Stokes, J. R. Moreno, E. A. Pnevmatikakis, and G. Carleo, Phases of two-dimensional spinless lattice fermions with first-quantized deep neural-network quantum states, *Physical Review B* **102**, 10.1103/physrevb.102.205122 (2020).
- [23] J. Hermann, J. Spencer, K. Choo, A. Mezzacapo, W. M. C. Foulkes, D. Pfau, G. Carleo, and F. Noé, Ab-initio quantum chemistry with neural-network wavefunctions (2022), arXiv:2208.12590 [physics.chem-ph].
- [24] G. Pescia, J. Nys, J. Kim, A. Lovato, and G. Carleo, Message-passing neural quantum states for the homogeneous electron gas, arXiv preprint arXiv:2305.07240 (2023), arXiv:2305.07240 [quant-ph].
- [25] J. Kim, G. Pescia, B. Fore, J. Nys, G. Carleo, S. Gandolfi, M. Hjorth-Jensen, and A. Lovato, Neural-network quantum states for ultra-cold fermi gases, arXiv preprint arXiv:2305.08831 (2023), arXiv:2305.08831 [cond-mat.quant-gas].
- [26] D. Pfau, J. S. Spencer, A. G. D. G. Matthews, and W. M. C. Foulkes, Ab initio solution of the many-electron schrödinger equation with deep neural networks, *Physical Review Research* **2**, 10.1103/physrevresearch.2.033429 (2020).
- [27] J. Hermann, Z. Schätzle, and F. Noé, Deep-neural-network solution of the electronic schrödinger equation, *Nature Chemistry* **12**, 891 (2020).
- [28] J. Nys and G. Carleo, Variational solutions to fermion-to-qubit mappings in two spatial dimensions, *Quantum* **6**, 833 (2022).
- [29] R. Jastrow, Many-body problem with strong forces, *Phys. Rev.* **98**, 1479 (1955).
- [30] R. P. Feynman and M. Cohen, Energy spectrum of the excitations in liquid helium, *Phys. Rev.* **102**, 1189 (1956).
- [31] M. Holzmann, D. M. Ceperley, C. Pierleoni, and K. Esler, Backflow correlations for the electron gas and metallic hydrogen, *Phys. Rev. E* **68**, 046707 (2003).
- [32] M. Holzmann and S. Moroni, Orbital-dependent backflow wave functions for real-space quantum monte carlo, *Phys. Rev. B* **99**, 085121 (2019).
- [33] P. López Ríos, A. Ma, N. D. Drummond, M. D. Towler, and R. J. Needs, Inhomogeneous backflow transformations in quantum monte carlo calculations, *Phys. Rev. E* **74**, 066701 (2006).
- [34] L. F. Tocchio, F. Becca, A. Parola, and S. Sorella, Role of backflow correlations for the nonmagnetic phase of the $t-t'$ hubbard model, *Phys. Rev. B* **78**, 041101 (2008).
- [35] L. F. Tocchio, F. Becca, and C. Gros, Backflow correlations in the hubbard model: an efficient tool for the metal-insulator transition and the large- u limit, *Physical Review B* **83**, 10.1103/physrevb.83.195138 (2011).
- [36] Y. Kwon, D. M. Ceperley, and R. M. Martin, Effects of three-body and backflow correlations in the two-dimensional electron gas, *Phys. Rev. B* **48**, 12037 (1993).
- [37] Y. Kwon, D. M. Ceperley, and R. M. Martin, Effects of backflow correlation in the three-dimensional electron gas: Quantum monte carlo study, *Physical Review B* **58**, 6800 (1998).
- [38] M. Hutcheon, Stochastic nodal surfaces in quantum monte carlo calculations, *Physical Review E* **102**, 10.1103/physreve.102.042105 (2020).
- [39] D. Luo and B. K. Clark, Backflow transformations via neural networks for quantum many-body wave functions, *Physical Review Letters* **122**, 10.1103/physrevlett.122.226401 (2019).
- [40] H. Lange, F. Döschl, J. Carrasquilla, and A. Bohrdt, Neural network approach to quasiparticle dispersions in doped antiferromagnets (2023), arXiv:2310.08578 [cond-mat.str-el].
- [41] T. Vieijra and J. Nys, Many-body quantum states with exact conservation of non-abelian and lattice symmetries through variational monte carlo, *Physical Review B* **104**, 10.1103/physrevb.104.045123 (2021).
- [42] T. Vieijra, C. Casert, J. Nys, W. De Neve, J. Haegeman, J. Ryckebusch, and F. Verstraete, Restricted boltzmann machines for quantum states with non-abelian or anyonic symmetries, *Physical Review Letters* **124**, 10.1103/physrevlett.124.097201 (2020).
- [43] T. Mizusaki and M. Imada, Quantum-number projection in the path-integral renormalization group method, *Physical Review B* **69**, 10.1103/physrevb.69.125110 (2004).
- [44] S. Morita, R. Kaneko, and M. Imada, Quantum spin liquid in spin 1/2 j_1 - j_2 heisenberg model on square lattice: Many-variable variational monte carlo study combined with quantum-number projections, *Journal of the Physical Society of Japan* **84**, 024720 (2015).
- [45] Y. Nomura, Helping restricted boltzmann machines with quantum-state representation by restoring symmetry, *Journal of Physics: Condensed Matter* **33**, 174003 (2021).
- [46] K. Choo, G. Carleo, N. Regnault, and T. Neupert, Symmetries and many-body excitations with neural-network quantum states, *Physical Review Letters* **121**, 10.1103/physrevlett.121.167204 (2018).
- [47] M. Y. Pei and S. R. Clark, Compact neural-network quantum state representations of jastrow and stabilizer states, *Journal of Physics A: Mathematical and Theoretical* **54**, 405304 (2021).
- [48] D. Pfau, S. Axelrod, H. Sutterud, I. von Glehn, and J. S. Spencer, Natural quantum monte carlo computation of excited states (2023), arXiv:2308.16848.
- [49] T. S. Cohen and M. Welling, Group equivariant convolutional networks (2016), arXiv:1602.07576 [cs.LG].
- [50] C. Roth and A. H. MacDonald, Group convolutional neural networks improve quantum state accuracy (2021), arXiv:2104.05085 [quant-ph].
- [51] C. Roth, A. Szabó, and A. MacDonald, High-accuracy variational monte carlo for frustrated magnets with deep neural networks (2023), arXiv:2211.07749 [cond-mat.str-el].
- [52] J.-H. Jung and J. D. Noh, Guide to exact diagonalization study of quantum thermalization, *Journal of the Korean Physical Society* **76**, 670 (2020).
- [53] L. Lam and A. Bunde, Phase transitions and dynamics of superionic conductors, *Zeitschrift für Physik B Condensed Matter* **30**, 65 (1978).
- [54] S. M. Girvin, Critical conductivity of the lattice gas, *Journal of Physics C: Solid State Physics* **11**, L751 (1978).
- [55] W. Czart, S. Robaszkiewicz, and B. Tobijaszewska,

- Charge ordering and phase separations in the spinless fermion model with repulsive intersite interaction, *Acta Physica Polonica Series a* **114**, 129 (2008).
- [56] E. Dagotto, T. Hotta, and A. Moreo, Colossal magnetoresistant materials: the key role of phase separation, *Physics Reports* **344**, 1 (2001).
- [57] H. J. Schulz, Correlation exponents and the metal-insulator transition in the one-dimensional hubbard model, *Phys. Rev. Lett.* **64**, 2831 (1990).
- [58] C. L. Henley and N.-G. Zhang, Spinless fermions and charged stripes at the strong-coupling limit, *Physical Review B* **63**, 10.1103/physrevb.63.233107 (2001).
- [59] N. G. Zhang and C. L. Henley, Stripes and holes in a two-dimensional model of spinless fermions or hardcore bosons, *Phys. Rev. B* **68**, 014506 (2003).
- [60] K.-H. Ma and N.-H. Tong, Interacting spinless fermions on the square lattice: Charge order, phase separation, and superconductivity, *Physical Review B* **104**, 10.1103/physrevb.104.155116 (2021).
- [61] G. Partridge, W. Li, Y. Liao, and R. Hulet, Pairing, phase separation, and deformation in the bec-bcs crossover, *Journal of Low Temperature Physics* **148**, 323 (2007).
- [62] A. Moreo and D. J. Scalapino, Cold attractive spin polarized fermi lattice gases and the doped positive u hubbard model, *Phys. Rev. Lett.* **98**, 216402 (2007).
- [63] J. E. Gubernatis, D. J. Scalapino, R. L. Sugar, and W. D. Toussaint, Two-dimensional spin-polarized fermion lattice gases, *Phys. Rev. B* **32**, 103 (1985).
- [64] D. J. Scalapino, R. L. Sugar, and W. D. Toussaint, Monte carlo study of a two-dimensional spin-polarized fermion lattice gas, *Phys. Rev. B* **29**, 5253 (1984).
- [65] J. de Woul and E. Langmann, Partially gapped fermions in 2d, *Journal of Statistical Physics* **139**, 1033 (2010).
- [66] J.-P. Song and R. T. Clay, Monte carlo simulations of two-dimensional fermion systems with string-bond states, *Phys. Rev. B* **89**, 075101 (2014).
- [67] O. Sikora, H.-W. Chang, C.-P. Chou, F. Pollmann, and Y.-J. Kao, Variational monte carlo simulations using tensor-product projected states, *Phys. Rev. B* **91**, 165113 (2015).
- [68] P. Corboz, R. Orús, B. Bauer, and G. Vidal, Simulation of strongly correlated fermions in two spatial dimensions with fermionic projected entangled-pair states, *Phys. Rev. B* **81**, 165104 (2010).
- [69] H. G. Evertz, The loop algorithm, *Advances in Physics* **52**, 1–66 (2003).
- [70] Z. Dai, Y. Wu, T. Wang, and M. P. Zaletel, Fermionic isometric tensor network states in two dimensions (2022), arXiv:2211.00043 [cond-mat.str-el].
- [71] T. Giamarchi, *Quantum Physics in One Dimension* (Oxford University Press, 2003) pp. 160–190.
- [72] R. Jördens, N. Strohmaier, K. Günter, H. Moritz, and T. Esslinger, A mott insulator of fermionic atoms in an optical lattice, *Nature* **455**, 204 (2008).
- [73] S. Fratini and J. Merino, Unconventional metallic conduction in two-dimensional hubbard-wigner lattices, *Phys. Rev. B* **80**, 165110 (2009).
- [74] M. Greiner, O. Mandel, T. Esslinger, T. Haensch, and I. Bloch, Quantum phase transition from a superfluid to a mott insulator in a gas of ultracold atoms, *Nature* **415**, 39 (2002).
- [75] K. Driscoll, Long-range Coulomb interactions and charge frustration in strongly correlated quantum matter (2022).
- [76] C. Mocanu, Bosonization of dimerized spinless-fermion and hubbard chains (2005), arXiv:cond-mat/0505238 [cond-mat.str-el].
- [77] L. Dang, M. Boninsegni, and L. Pollet, Vacancy supersolid of hard-core bosons on the square lattice, *Phys. Rev. B* **78**, 132512 (2008).
- [78] A. B. Khanikaev, A. V. Baryshev, M. Inoue, A. B. Granovsky, and A. P. Vinogradov, Two-dimensional magnetophotonic crystal: Exactly solvable model, *Phys. Rev. B* **72**, 035123 (2005).
- [79] K.-T. Chen and Y.-J. Chiu, Spinless fermions with repulsive interactions (2010).
- [80] F. Mila, Exact result on the mott transition in a two-dimensional model of strongly correlated electrons, *Phys. Rev. B* **49**, 14047 (1994).
- [81] D. Wu, R. Rossi, F. Vicentini, N. Astrakhantsev, F. Becca, X. Cao, J. Carrasquilla, F. Ferrari, A. Georges, M. Hibat-Allah, M. Imada, A. M. Läuchli, G. Mazzola, A. Mezzacapo, A. Millis, J. R. Moreno, T. Neupert, Y. Nomura, J. Nys, O. Parcollet, R. Pohle, I. Romero, M. Schmid, J. M. Silvester, S. Sorella, L. F. Tocchio, L. Wang, S. R. White, A. Wietek, Q. Yang, Y. Yang, S. Zhang, and G. Carleo, Variational benchmarks for quantum many-body problems (2023), arXiv:2302.04919 [quant-ph].
- [82] G. Carleo, K. Choo, D. Hofmann, J. E. Smith, T. Westerhout, F. Alet, E. J. Davis, S. Efthymiou, I. Glasser, S.-H. Lin, M. Mauri, G. Mazzola, C. B. Mendl, E. van Nieuwenburg, O. O'Reilly, H. Théveniaut, G. Torlai, F. Vicentini, and A. Wietek, NetKet: A machine learning toolkit for many-body quantum systems, *SoftwareX* **10**, 100311 (2019).
- [83] F. Vicentini, D. Hofmann, A. Szabó, D. Wu, C. Roth, C. Giuliani, G. Pescia, J. Nys, V. Vargas-Calderón, N. Astrakhantsev, and G. Carleo, NetKet 3: Machine Learning Toolbox for Many-Body Quantum Systems, *SciPost Phys. Codebases*, 7 (2022).
- [84] S. Sorella, Generalized lanczos algorithm for variational quantum monte carlo, *Phys. Rev. B* **64**, 024512 (2001).
- [85] K. He, X. Zhang, S. Ren, and J. Sun, Deep residual learning for image recognition (2015), arXiv:1512.03385 [cs.CV].
- [86] C. Trabelsi, O. Bilaniuk, Y. Zhang, D. Serdyuk, S. Subramanian, J. F. Santos, S. Mehri, N. Rostamzadeh, Y. Bengio, and C. J. Pal, Deep complex networks (2018), arXiv:1705.09792 [cs.NE].
- [87] A. Dhar, J. J. Kinnunen, and P. Törmä, Population imbalance in the extended fermi-hubbard model, *Physical Review B* **94**, 10.1103/physrevb.94.075116 (2016).
- [88] P. T. Brown, D. Mitra, E. Guardado-Sanchez, P. Schauß, S. S. Kondov, E. Khatami, T. Paiva, N. Trivedi, D. A. Huse, and W. S. Bakr, Spin-imbalance in a 2d fermi-hubbard system, *Science* **357**, 1385 (2017).
- [89] C. S. Chiu, G. Ji, A. Bohrdt, M. Xu, M. Knap, E. Demler, F. Grusdt, M. Greiner, and D. Greif, String patterns in the doped hubbard model, *Science* **365**, 251 (2019).

Appendix A: Numerical details and backflow architecture

Given a set of occupation numbers, our symmetrized wavefunction ansatz is expressed as in Eq. (7), where

we use a translation-invariant Jastrow factor defined in Eq. (3) with variational parameters $\theta_J = W_{d(ij)}$. The mean-field orbitals are captured by the matrix $M_{\mu,i}$ as defined in Eq. (1) of variational parameters of size $N_f \times N_s$. The backflow corrections are constructed as a translational equivariant convolutional neural network with parameters θ_{BF} .

The total set of variational parameters $\theta = (M_{\mu,i}, \theta_{BF}, \theta_J)$ are all optimized simultaneously using Variational Monte Carlo and Stochastic Reconfiguration [84]. To accelerate the optimization convergence of our Neural Slater-Backflow-Jastrow ansatz, we initialize the orbital parameters with converged parameters of a Hartree-Fock optimization.

For smaller systems (i.e. $L = 4$) we use shallow backflow CNN networks with one hidden layer and 32 features. For larger and more challenging systems such as $L = 8, 10$ we construct a residual CNN with 5 convolutional layers and 16 features per filter. Residual networks make the training more stable [22, 51, 85]. To access low-lying energy states, we use the latter residual CNN architecture regardless of the system size. Our deep CNNs use complex-valued weights for the feature maps. Each layer, except the final one, uses the complex Rectified Linear Unit (ReLU) activation function [86]. The output layer produces the backflow functions necessary for our computations.

We optimize multiple CNN backflow transformation models in parallel, corresponding to the N_f orbitals, ensuring efficient and scalable processing.

Appendix B: Density-density Correlation Function

To complement the results for $L = 10$ shown in Fig. 4 (a), we also present the density-density correlation function, as defined in Eq. 11, for a system size of $L = 8$ and $\bar{n} = 0.44$ in Fig. 11. Similar to the $L = 10$ case, we observe that the correlations display more pronounced oscillations as V/t increases, indicating the increasing orderliness of the charge distribution during the phase transition. This behavior suggests a stronger tendency towards charge ordering with increasing interaction strength. In the charge-ordered (CO) phase, the amplitude of the oscillations gradually diminishes with distance. Conversely, in the metallic phase, the oscillations diminish more quickly with distance, highlighting a less ordered charge distribution. For weak couplings, correlations exhibit minimal oscillations and fade as the graph distance R increases.

Appendix C: Excitation spectrum for closed-shell $L = 10$ case

In Fig. 12, we display the energy spectrum for $L = 10$ and a closed-shell density $\bar{n} = 0.41$, across different symmetry sectors for varying V/t . Similar to the $L = 8$

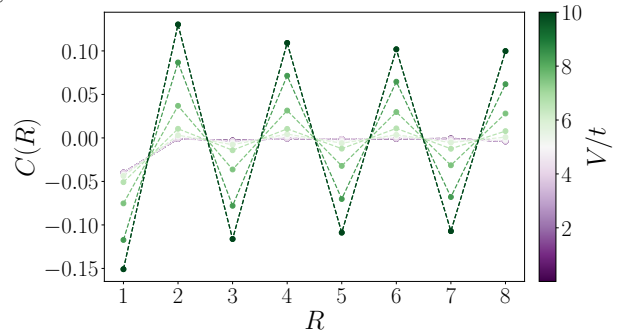


FIG. 11. The two-point density-density correlation functions as a function of graph distance R for different values of V/t for a system size of $L = 8$ and $\bar{n} = 0.44$.

case presented in the main text (Fig. 7), we observe that the ground state is situated within the \mathbf{K} sector.

As in the previous case, we also compare our symmetrized Neural Slater-Backflow-Jastrow (ψ_{BF}^K) ansatz with a symmetrized Slater-Jastrow (ψ^K) ansatz without backflow, and observe improved energy levels, even for low-lying excited states, with the inclusion of the backflow correction term, especially for larger V/t values.

Appendix D: Excitation Structure for Open-shell $L = 4$ case

Moving away from closed shells induces changes in the structure of the excitation energies [87–89]. In Fig. 13, we benchmark our ansatz for the $L = 4$ system with $\bar{n} = 0.44$, which is not a closed-shell system. In the top panel, we compute the lowest and second-lowest energies using ED methods in each assigned \mathbf{K} sector and compare the lowest energies in each sector to our VMC ansatzes. In the lower panel, we present the corresponding relative errors of the ansatzes. Our results show that the symmetric backflow improves the accuracy, demonstrating that our ansatz can also be effectively applied to non-closed-shell systems for computing excited states.

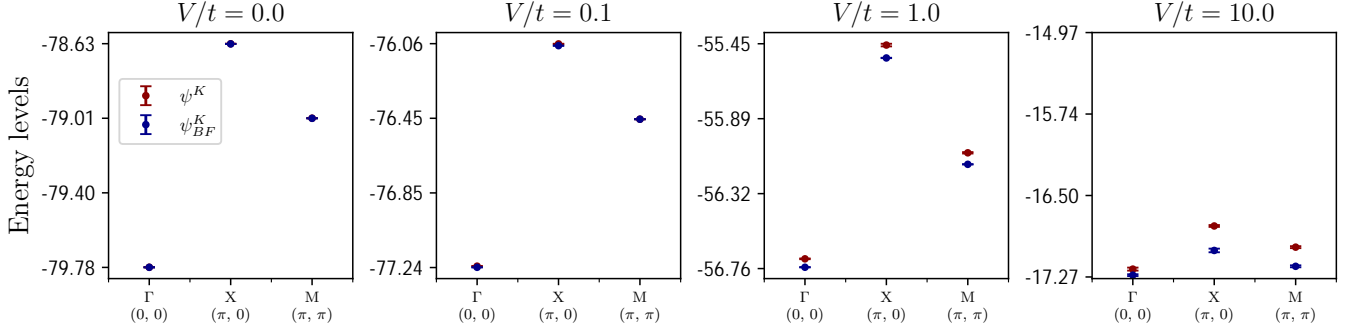


FIG. 12. Lowest excitation energies in different \mathbf{K} sectors for an $L = 10$ closed-shell system with $\bar{n} = 0.41$, comparing different VMC ansatz.

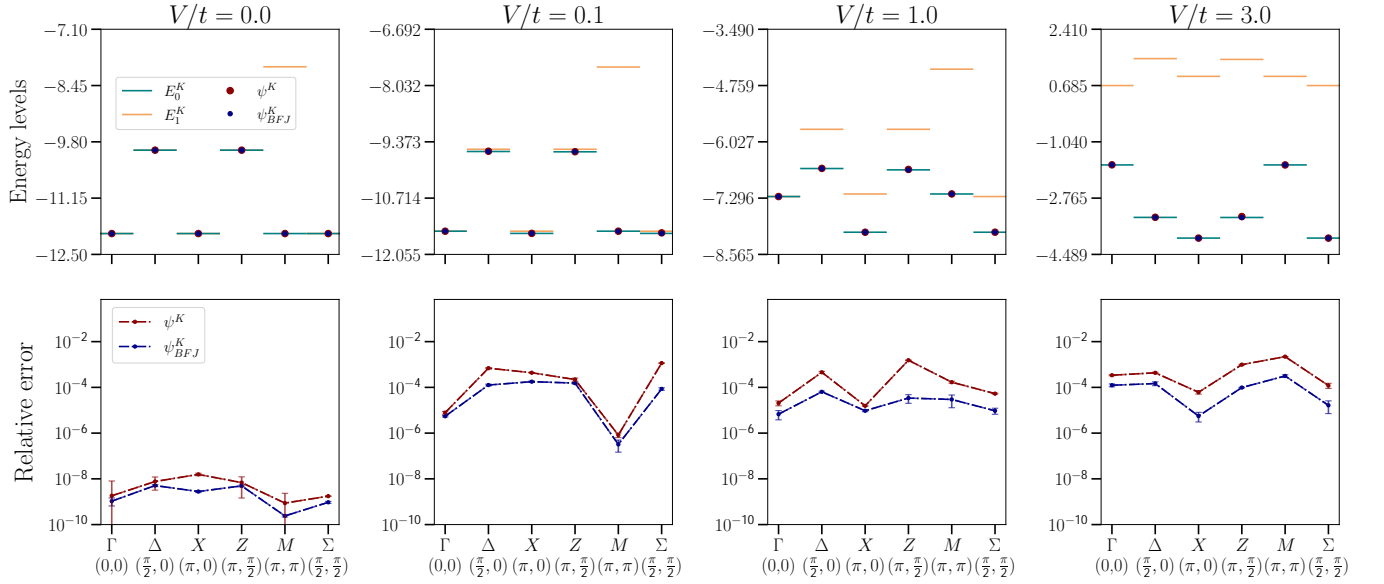


FIG. 13. In the upper row, we compute the lowest and second-lowest energies for the designated \mathbf{K} sector using ED and compare the lowest energies with our VMC ansatzes. The dashed lines in the lower row represent the relative errors of the ansatzes. These results correspond to an $L = 4$ system for $\bar{n} = 0.44$, which is not a closed-shell system.